

Article

A Thermodynamic Comparison of Nanotip and Nanoblade Geometries for Ultrafast Laser Field Emission via the Finite Element Method

Joshua Mann *  and James Rosenzweig

Department of Physics and Astronomy, University of California, Los Angeles, CA 90095, USA;
rosen@physics.ucla.edu

* Correspondence: jomann@physics.ucla.edu

Abstract: Strong laser field emission from metals is a growing area of study, owing to its applications in high-brightness cathodes and potentially as a high harmonic generation source. Nanopatterned plasmonic cathodes localize and enhance incident laser fields, reducing the spot size and increasing the current density. Experiments have demonstrated that the nanoblade structure outperforms nanotips in the peak fields achieved before damage is inflicted. With more intense surface fields come brighter emissions, and thus investigating the thermomechanical properties of these structures is crucial in their characterization. We study, using the finite element method, the electron and lattice temperatures for varying geometries, as well as the opening angles, peak surface fields, and apex radii of curvature. While we underestimate the energy deposited into the lattice here, a comparison of the geometries is still helpful for understanding why one structure performs better than the other. We find that the opening angle—not the structure dimensionality—is what primarily determines the thermal performance of these structures.

Keywords: finite element method (FEM); ultrafast; laser field emission; two-temperature model; damage threshold; nanostructure; rescattering; plasmonics



Citation: Mann, J.; Rosenzweig, J. A Thermodynamic Comparison of Nanotip and Nanoblade Geometries for Ultrafast Laser Field Emission via the Finite Element Method. *Physics* **2024**, *6*, 1–12. <https://doi.org/10.3390/physics6010001>

Received: 6 October 2023

Revised: 7 November 2023

Accepted: 28 November 2023

Published: 19 December 2023



Copyright: © 2023 by the authors. Licensee MDPI, Basel, Switzerland. This article is an open access article distributed under the terms and conditions of the Creative Commons Attribution (CC BY) license (<https://creativecommons.org/licenses/by/4.0/>).

1. Introduction

Nanostructured cathodes have been utilized in electron microscopes [1], ultra-fast (low-energy) electron diffraction [2], and electron guns [3]. They are hailed for their high brightness and, in the case of metals, ultra-fast response times. Using a nanostructure such as a nanotip or a nanoblade enhances and confines the incident laser fields to the apex. This increases the current density, thereby improving the brightness. However, this process is limited by the structure's ability to withstand intense illumination. Nanotips tend to break down in enhanced ultra-fast laser fields exceeding 10 V/nm [4,5], whereas nanoblades appear to attain surface fields of at least 40 V/nm [6] and likely up to 80 V/nm [7] according to the peak electron energies observed. A higher surface field leads to a larger current density and therefore a higher beam brightness [8]. Finding ways of improving thermomechanical survivability—for any structure—is therefore critical for improving the brightness in ultrafast cathodes.

Under laser illumination, energy is absorbed predominantly by the electron population. Electrons near the apex disperse energy on a timescale from a few to 10 s of femtoseconds, which is effectively instant. They then disperse energy throughout the bulk on a scale from 10 s to 100 s of femtoseconds [9]. However, a heated electron gas does not directly damage the material. Such damage would be caused by movements of the ions in the lattice, and thus the lattice temperature (the temperature of the phonon gas) is a better proxy for indicating damage. As electron-phonon scattering occurs on picosecond timescales, ultrafast illumination results in a thermal non-equilibrium, with the electrons attaining a higher temperature than the lattice. This known phenomenon has therefore been treated

using two-temperature models [10]. Thus, if the laser pulse is short on the electron-phonon timescale, then the electrons disperse a substantial portion of the deposited energy before the lattice can absorb it.

In our previous analysis [9], we studied these timescales with simple geometric models to show that the dimensionality of the structure is the determining factor for how well it disperses energy; that is, the nanoblade effectively has two dimensions it may disperse energy through, while the tip only has one (for exceptionally small opening angles), and therefore the blade would more readily disperse deposited energy. As we find in the present analysis, this was actually a partially incorrect sentiment. To obtain a more accurate conclusion, we aim to accurately model the geometries using the finite element method (FEM). This removes the “fictitious apex” problem which had plagued the simple geometric analysis. Inclusion of both the electron and lattice temperatures is then straightforward as well, leading to a more complete model.

2. Materials and Methods

In this study, we solve the two-temperature heat equation for solid gold nanotips and nanoblades. We singled out gold because previous nanoblade studies have considered gold coated blades [7–9]. The heat equations follow:

$$\begin{aligned} \frac{C_e(T_e)}{2T_e} \partial_t T_e^2 &= \frac{K_e(T_e)}{2T_e} \nabla^2 T_e^2 - g(T_e - T_l) + S(r, t), \\ C_l(T_l) \partial_t T_l &= \nabla \cdot (K_l(T_l) \nabla T_l) + g(T_e - T_l). \end{aligned} \quad (1)$$

We use the free electron gas (FEG) model for the electronic thermal capacity and conductivity, $C_e = \gamma T_e$ and $K_e = K_{e0} T_e / T_{l0}$ (with $\gamma = 71.5 \text{ Jm}^{-3} \text{ K}^{-2}$ and $K_{e0} = 310 \text{ Wm}^{-1} \text{ K}^{-1}$) [11,12]. Here, T_e and T_l denote the electron and lattice temperatures, respectively, $S(r, t)$ represents the surface heating function, g is the electron-phonon coupling constant, r is the spatial coordinate, t is the time, and $\partial_t \equiv \partial / \partial t$. It is then natural to translate this to the provided temperature-squared electron heat equation.

In the current analysis, lattice heating is entirely attributed to heat transfer from the thermalized electron distribution via electron-phonon scattering. The electron-phonon coupling constant g varies from material to material and for differing temperatures [13]. According to Figure 4d in Ref. [13], and by extrapolation, for electron temperatures up to 30,000 K, the coupling constant in gold is less than $g = 3 \times 10^{17} \text{ Wm}^{-3} \text{ K}^{-1}$, and therefore we use this approximate constant value. On the whole, this leads to an overestimation of the lattice heating for cool electron temperatures but is somewhat accurate at high temperatures. We additionally run calculations for $g = 0.2 \times 10^{17} \text{ Wm}^{-3} \text{ K}^{-1}$ (a low temperature limit; see Appendix C). This alteration does not affect our conclusions. Similarly, the electron thermal capacity increases beyond being linear (and one expects a similar increase for the electron thermal conductivity), but to retain the simpler temperature-squared heat equation, we continue with the simpler linear approximation.

The lattice thermal conductivity and capacity follow from the Debye model [14,15]. For computational purposes, we integrate by parts to find the final forms which are efficiently implemented in the code:

$$\begin{aligned} C_l(T_l) &= 9k_b n \left[-\frac{x}{e^x - 1} + \frac{4}{3} D_3(x) \right] \\ K_l(T_l) &= k_b \left(\frac{\pi n^2}{6} \right)^{1/3} \sum_i v_i \left[-\frac{x_i}{e^{x_i} - 1} + \frac{3}{2} D_2(x_i) \right] \end{aligned} \quad (2)$$

with $i \in \{L, T\}$ the longitudinal and transverse sound modes respectively (the transverse mode is doubly counted), the relative Debye temperature, $x_i = \Theta_{Di} / T_l$, the number density of atoms, $n = 5.91 \times 10^{28} \text{ m}^{-3}$, the transverse and longitudinal sound velocities, $v_T = 1200 \text{ m/s}$ and $v_L = 3240 \text{ m/s}$ [16], respectively, and the Debye functions

$D_N(x) = \frac{n}{x^N} \int_0^x dt \frac{t^N}{e^t - 1}$. In the conductivity formula, the modal Debye temperatures are calculated via the sound velocity [15] and are $\Theta_{DT} = 139.16$ K and $\Theta_{DL} = 375.74$ K. For the heat capacity, we use the Debye temperature for gold from the literature: $\Theta_D = 170$ K.

2.1. Linear Dielectric Heating

For the nanoblade structure, part of the field enhancement may be attributed to traveling surface plasmon polaritons (SPPs) which trail the laser as it traverses the length of the blade. This invites a simpler linear analysis for low fields. For a given frequency, each material has a complex dielectric constant, with the imaginary component indicating loss of energy into the material. The SPP wavevector, k , and longitudinal decay constant, κ , may be found from the dielectric constant:

$$k = \frac{\omega}{c} \left(\frac{\epsilon_r}{\epsilon_r + 1} \right)^{1/2}, \quad \kappa = \frac{\omega}{c} \left(\frac{\epsilon_r}{\epsilon_r + 1} \right)^{3/2} \frac{\epsilon_i}{2\epsilon_r^2}, \quad (3)$$

where ω denotes the wave frequency, c denotes the speed of light, and $\epsilon_r = -25$ and $\epsilon_i = 1.25$ are the approximate real and imaginary relative permittivities at the laser wavelength 800 nm, respectively [17]. The electron temperatures in our analysis exceed 30,000 K, necessitating the inclusion of a variable dielectric constant. Such considerations increase the heating and peak lattice temperatures [18]. The nonlinear $U_p \approx 50$ eV-scale dynamics of the constituent electrons within the SPPs at 80 V/nm further complicate this consideration (with U_p being the ponderomotive energy of the field). Here, we continue with constant dielectric constants as we only compare the performance of these structures. Some of the nonlinear contributions are accounted for by vacuum heating in Section 2.2 below.

The SPP group velocity, $v_g = \partial\omega/\partial k = c(1 + 1/\epsilon_r)^{1/2}$, associated with this dispersion relation is the speed at which bound electromagnetic energy traverses the surface. Therefore, the dielectric loss power density reads

$$S_d(r, t) = \frac{du}{dt} = \kappa v_g u, \quad (4)$$

where u is the electromagnetic energy surface density. For a surface plasmon polariton, this is given by

$$u = \frac{\epsilon_0 \kappa_{z1}^2}{2 k^2} E^2 \left[\frac{1}{2\kappa_{z1}} \left(\left(1 + \left(\frac{k}{\kappa_{z1}} \right)^2 \right) + \left(\frac{\omega}{\kappa_{z2}c} \right)^2 \right) + \frac{1}{2\kappa_{z2}} \left(\epsilon_r \left(1 + \left(\frac{k}{\kappa_{z2}} \right)^2 \right) + \left(\frac{\omega}{\kappa_{z2}c} \right)^2 \right) \right], \quad (5)$$

where $\kappa_{z1} = \sqrt{k^2 - \omega^2/c^2}$ and $\kappa_{z2} = \sqrt{k^2 - \epsilon_r \omega^2/c^2}$ are the spatial extent of the plasmon into a vacuum and into the material, respectively. Note that the dependence on the field is squared, and thus, as expected, the energy deposition rate is directly proportional to the intensity of the field.

2.2. Vacuum Heating

The above prescription accounts for low field perturbations. However, we are interested in reaching significantly high fields. We expect nonthermal carriers to account for the majority of lost energy present in the system by naively extrapolating Figure 4 in Ref. [10] to V/nm fields. This is a point of contention, and the extension of work of Ref. [10] to fields relevant for this analysis may serve as future work.

The nonthermal electrons in the system considered here arise from the vacuum dynamics of the quasi-free surface plasma. This plasma undergoes ponderomotive motion in the enhanced laser field, with most of the charge returning to the material and transmitting into bulk. Therefore, one may just sum up much of the deposited energy at a high field by studying the near-field dynamics. This is precisely the work in Ref. [19], where a heating intensity was found:

$$S_v(r, t) = \frac{du}{dt} = \frac{\eta \epsilon_0}{4\pi} v_{\text{osc}} E^2, \quad (6)$$

with $\eta \approx 1.57$ being a numerically attained constant and ϵ_0 denoting the vacuum electric permittivity. The ponderomotive velocity is given by $v_{osc} = \frac{e}{m_e \omega} E$, where m_e denotes the electron mass. Thus, the energy deposition rate is proportional to the laser intensity to the power of $3/2$. For the chosen values, vacuum heating locally surpasses linear (temperature-independent) dielectric heating at $E \approx 40$ V/nm.

The energy in this model is carried initially by nonthermal electrons. However, electrons in a good conductor (aluminum) and within the energy range from 2 eV to 500 eV (which encompasses any electron undergoing such ponderomotive motion for the fields we consider) have a range of less than 10 nm [20]. Therefore, the energy in this analysis is deposited essentially throughout the apex. The thermalized electron distribution effectively approaches equilibrium instantly at this length scale and on all other timescales [9]. Thus, only direct heating of the lattice by nonthermal electrons and plasma heating beyond that which we cover here remain as contenders for damaging effects, which we leave for a future investigation.

2.3. Finite Element Method Set-Up

We create meshes modeling the nanoblade and nanotip structures using Gmsh [21] and solve for the electron and lattice temperature over time with the FEM using SfePy [22].

Figure 1 shows a 2-dimensional (2D) cross-section of the blade and tip structures. The nanoblade geometry is created with a circle of a radius R embedded in a 2D wedge with a half-opening angle θ such that the wedge and circle are tangent to each other, and any wedge above the tangent point is removed. The center of the circle is $10R$ above the bottom of the wedge. To test for accuracy, we double this height and observe a peak lattice temperature difference of only up to 33.5 K (see Appendix A). By symmetry, only the right-hand side of the 2D slice is needed. We use nearly the same recipe for the nanotip, with the difference being that the 2D slice is revolved about the central axis by 90 deg to create a tip quadrant.

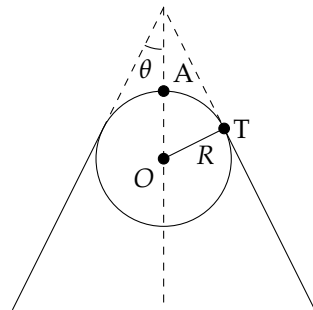


Figure 1. Cross-section of the nanoblade and nanotip geometries. We represent the nanoblade using the right half of this 2-dimensional (2D) representation and the tip by revolving that 2D half about the vertical axis by 90 deg. We denote with A the apex of the structure and T the tangent point. The apex has a radius of curvature of R and an opening angle of θ .

The local grid size (set when creating the points used to define the above geometries) is set to $0.1 \times R$ for the blade and $0.5 \times R$ for the tip. For the blade only, at the tangent point and at the apex, this value is refined to $0.05 \times R$ and $0.01 \times R$, respectively. The tip apex mesh is quite coarse, but this turns out to not be an issue (see Appendix A). The time step, dt , for the first 80 fs is 0.4 fs, and for the remaining 3920 fs (for a total simulation duration of 4000 fs), it is 19.6 fs.

We reduce the heat equations into their weak forms for the FEM calculation:

$$\int_{\Omega} d\Omega \left[\frac{\gamma}{2} s_e \frac{dT_e^2}{dt} + \frac{K_{e0}}{2T_{l0}} \nabla s_e \cdot \nabla T_e^2 + g(T_e - T_l) s_e \right] = \int_{\Gamma_{surf}} d\Gamma S(r, t) s_e, \tag{7}$$

$$\int_{\Omega} d\Omega \left[C_l s_l \frac{dT_l}{dt} + K_l \nabla s_l \cdot \nabla T_l - g(T_e - T_l) s_l \right] = 0$$

with s_e and s_l as the dummy variables associated with T_e^2 and T_l , respectively, Ω as the area/volume within the structure and Γ_{surf} as the facets in contact with vacuum.

The electron and lattice temperatures are initialized to 300 K. We assume that the structures are adhered by their bases to a heat bath at 300 K, necessitating an essential Dirichlet boundary condition on this facet for both distributions. The electron heating at the surface is accounted for within the weak form with a surface heating function $S(r, t)$. All other boundary conditions are of the Neumann type with zero flux (no heat traverses the metal–vacuum boundary or the symmetry planes), and the weak form naturally defaults to this condition when not otherwise specified.

The heating term includes a combination of the linear plasmonic loss and the nonlinear vacuum heating, where $S(r, t) = S_d(r, t) + S_v(r, t)$. However, both of these heating models are dependent on the local field strength $E(r, t)$. We choose the local field as a function of the position such that it mimics the fields we expect near these structures, akin to a conducting cylinder or sphere embedded in an otherwise uniform electric field. For points above the circle center and for $t < 4\tau$, where $\tau = 8$ fs is the full-width half-maximum of the field strength, one has:

$$E(r, t) = E_0 \sin^2\left(\frac{\pi t}{4\tau}\right) \cos\phi(r) e^{-\kappa_{z1}(|r|-R)}, \quad (8)$$

where E_0 is the peak surface field, $\sin^2(\cdot)$ is the pulse envelope, $\cos\phi$ is the field profile about the apex ($\phi = \angle AOr$ is the angle created from the vertical axis by a ray from the circle's center to the point r on the surface) and the exponential term diminishes the field intensity away from the apex. We choose κ_{z1} as a reasonable scale for the field drop off.

3. Results

3.1. Timescale Analysis

The timescales previously described are further illuminated by the temperature time plots in Figure 2 and the spacetime plots in Figure 3. These are for the nanoblade structure with $R = 20$ nm, $E_0 = 80$ V/nm and $\theta = 30$ deg, though all the cases we study here are qualitatively the same. Heating of the structure proceeds as follows: (I) On a scale of 10 s of femtoseconds, the illuminating laser heats up the electron distribution. As the laser turns off, the apex quickly comes to equilibrium, resulting in a slight dip in temperature. (II) On a scale of 100 s of femtoseconds, the electronic distribution continues to disperse energy throughout the bulk of the structure and deposits some energy into the lattice. (III) On a scale of picoseconds, the electrons have dispersed much of the thermal energy initially deposited, and the lattice has reached its peak temperature. The electron temperature is less than the lattice temperature, indicating that the electronic distribution is beginning to cool the apex. This sequence confirms that the electron heating and cooling processes are on quite different timescales from lattice heating and cooling.

3.2. Comparison of Structures

The primary result of this study is the comparison of the tip and blade structures. The apex lattice temperatures as a function of time for the blade and tip structures with $\theta = 3$ and 30 degrees are shown in Figure 4. The curves follow a qualitatively similar path by first heating, reaching a peak temperature and then slowly cooling. The structures corresponding most closely to real structures are the 3-degree tip and 30-degree blade. Here, one can immediately see that the realistic blade outperforms the realistic tip, albeit only by about 200 K.

The peak achieved lattice temperatures as a function of the peak surface field E_0 is shown in Figure 5 for the same structures shown above. As expected, the peak temperature increases monotonically with increasing field strength. Again, the realistic blade outperforms the realistic tip for the same field strengths. The “fictional” three-degree blade is the only structure which appears to reach the melting point here.

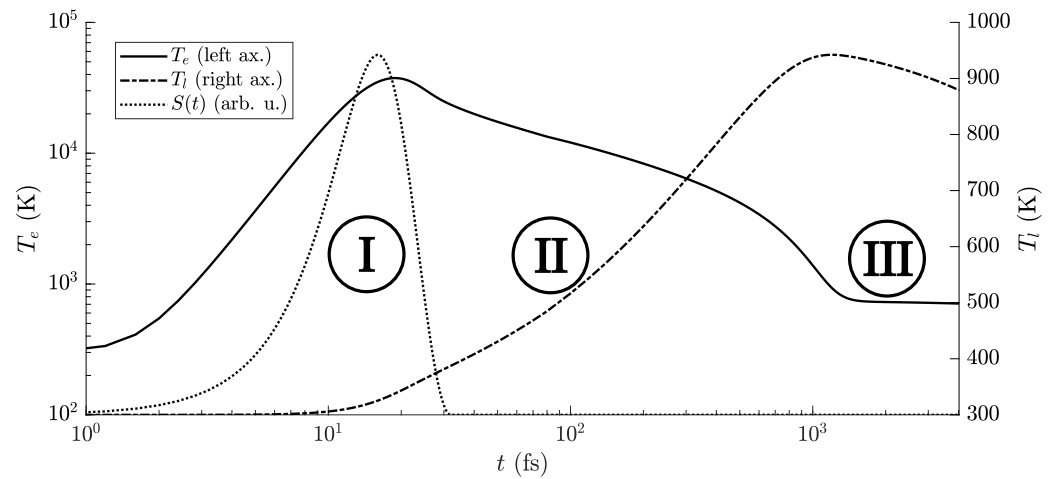


Figure 2. Time plots for the electron (solid) and lattice (dot-dashed) temperatures at the apex as well as the laser envelope (dotted) for the nanoblade structure with $R = 20$ nm, the peak surface field, $E_0 = 80$ V/nm, and $\theta = 30$ deg. (I) The laser heats up the electron distribution, and the apex comes to near-equilibrium. (II) The electronic distribution disperses energy throughout the bulk of the structure and begins to deposit energy into the lattice. (III) The electronic distribution has cooled to below the now-heated lattice temperature and begins to aid in cooling.

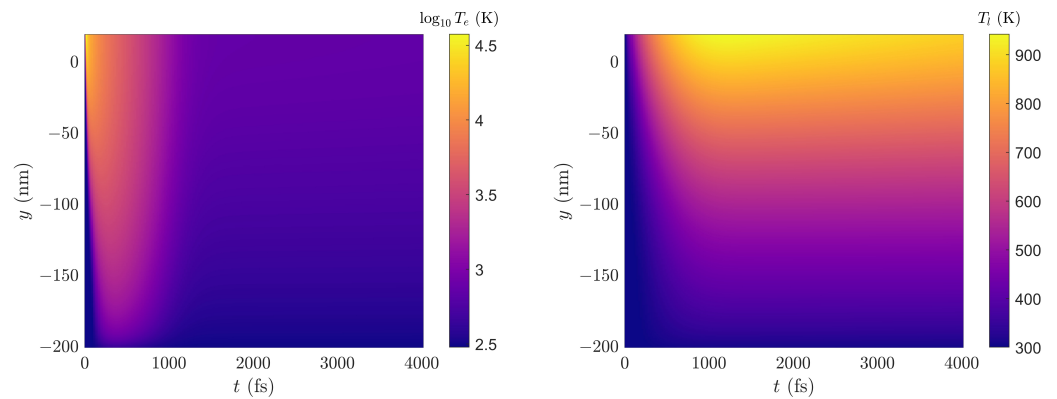


Figure 3. Spacetime plots for the electron (left) and lattice (right) temperatures for the nanoblade structure with $R = 20$ nm, $E_0 = 80$ V/nm and $\theta = 30$ deg. The curves in Figure 2 are these data evaluated at the apex at the maximal y value.

When sweeping over the opening angles instead, Figure 6 is quite illuminating. Here, we again used a peak field of 80 V/nm. It is now understandable that the blade structure does not outperform the tip in general. Actually, the tip appears to outperform the blade. At about $\theta = 4$ deg, the blade apex reaches the melting point of gold, while the tip does not reach it at all. For an increasing opening angle, the peak temperature drops drastically, indicating that the opening angle is the stronger independent variable.

Finally, by sweeping over the apex radius of curvature for the 30 deg blade at $E_0 = 80$ V/nm, we obtain Figure 7. The increasing apex size increases the total energy deposited into the structure, thereby increasing the peak lattice temperatures achieved. Even though the electron distribution within the apex still equilibrates rapidly, there is more thermal energy for essentially the same bulk structure below.

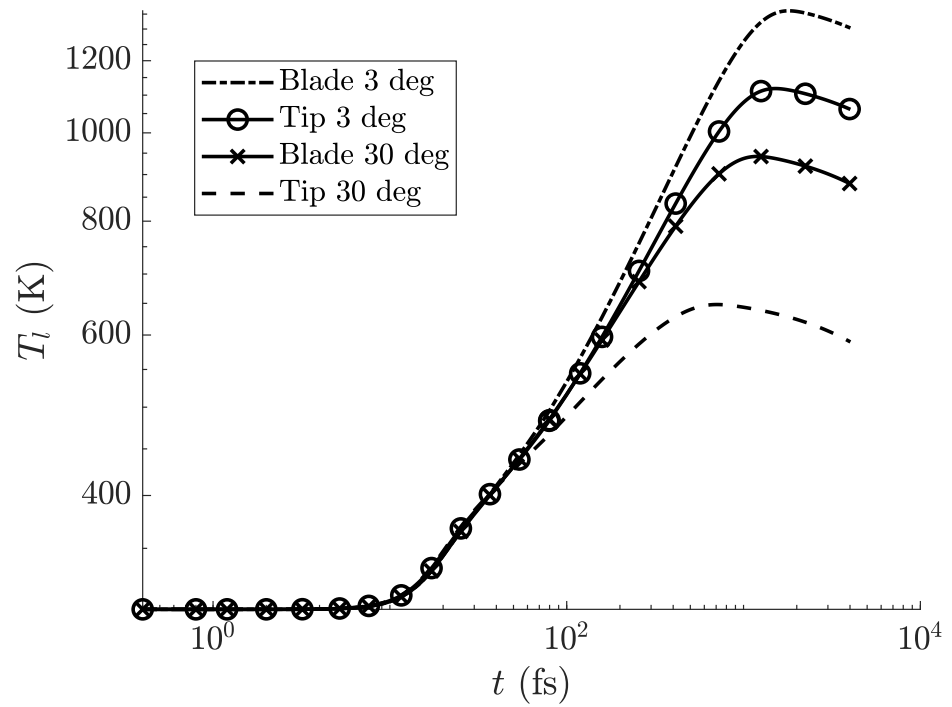


Figure 4. The lattice temperatures at the apex over time for structures with a 3 deg opening angle (blade: dot-dashed; tip: solid and circles) and for a 30 deg opening angle (blade: solid and crosses; tip: dashed). The peak field strength here is 80 V/nm. The structures corresponding most closely to real structures are the 3-degree tip and 30-degree blade. Note that the opening angle appears to have the strongest impact on peak achieved temperatures, followed by the dimensionality.

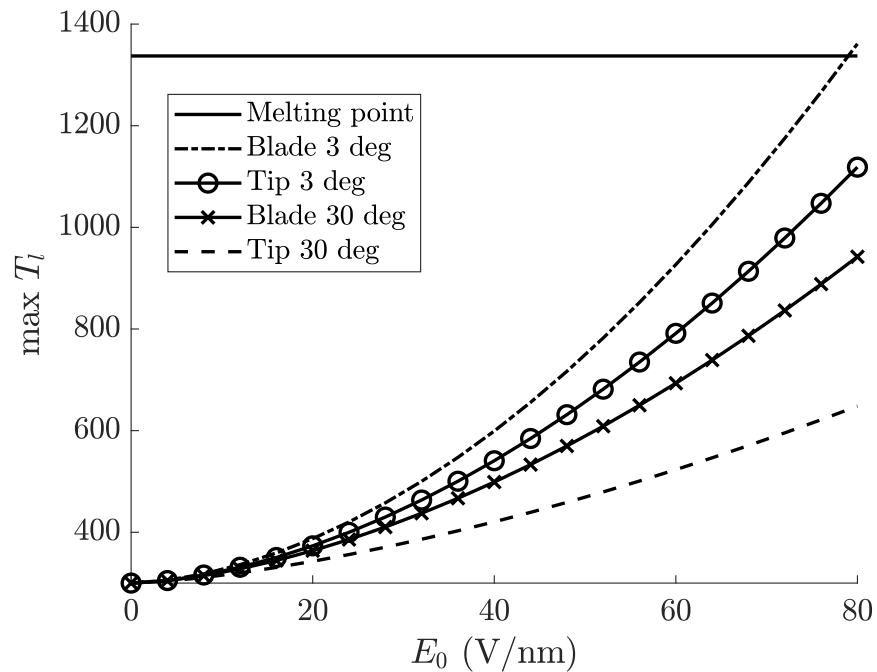


Figure 5. The peak lattice temperatures achieved as a function of the peak applied field. The 3-degree tip (solid and circles) reaches a higher temperature than the 30-degree blade (solid and crosses). The 30-degree tip (dashed) outperforms the other structures here, and the fictional 3-degree blade (dot-dashed) is the only structure here which heats to the melting point of gold (solid).

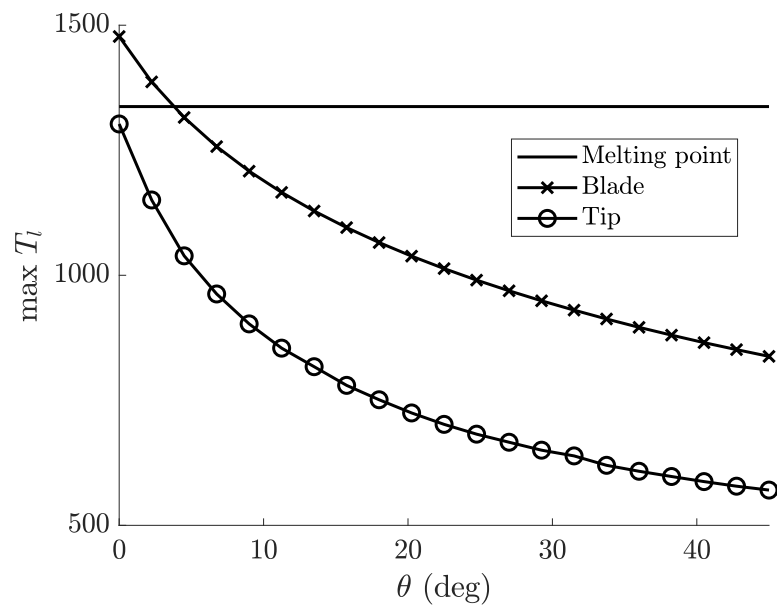


Figure 6. The peak lattice temperatures as a function of the opening angle θ for the blade (crosses) and tip (circles). Even for the same small opening angles, the blade becomes hotter than the tip. This further indicates that the opening angle strongly impacts thermal dissipation.

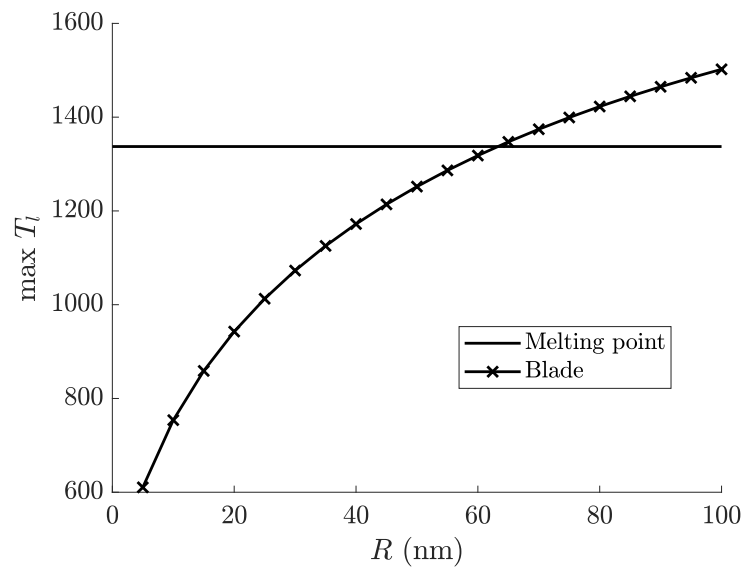


Figure 7. The peak lattice temperatures as a function of the apex radius R for the 30 deg blade (crosses) with $E_0 = 80 \text{ V/nm}$. Unfortunately, we could not perform the same sweep for the tips. The peak temperature increases as the apex size increases.

4. Discussion

In our previous study [9], we posited that the blade structure would outperform the tip structure thermomechanically as a consequence of its higher dimensionality. The blade may disperse energy effectively in two dimensions, while the tip only has one effective dimension, considering their typical small opening angles. Here, however, we found a different reason for their performance gap. Actually, for the same opening angles, the tip outperforms the blade.

This leads us to the conclusion that using a larger opening angle is a better avenue for improving thermals than using a different structure altogether. A pyramid structure [23], which is tip-like but with large enough opening angles, may achieve higher surface fields

and therefore higher brightness emissions with its larger opening angle. However, the pyramid structure retains quite a small interaction area, which may necessitate an array.

We were not able to accurately predict the damage thresholds here. As a matter of fact, we only predicted melting at the apex for quite narrow blades below 4 deg and for large apices. We also predicted tip survivability at fields up to 80 V/nm, which is certainly not realistic. Let us now discuss several ways in which this analysis may be built upon.

Firstly, the blade structure likely does not attain a bulk geometric enhancement that leads to 80 V/nm fields. Rather, these fields are likely obtained via hot spots [6]. Inclusion of these hot spots is of interest for this study. One would additionally need to model the electromagnetic and plasmonic fields to properly implement the hot spots. However, their inclusion ultimately reduces the heating of the structure compared with this smooth analysis. Any localized electronic heating at the hot spots quickly dissipates into the bulk of the apex according to the effectively instant relaxation time at these small scales [9], and thus one would not predict direct damage to these hot spots through this additional consideration alone.

We additionally used the FEG approximation for the electronic heat capacities and conductivities. These properties, as well as the electron-phonon coupling factor, are calculated by integrating over the density of states [13]. At energies about 2 eV \approx 20,000 K below the Fermi level, *d*-shell electrons begin to contribute to both these quantities. We achieved temperatures that extended beyond this range, and therefore inclusion of the density of states is necessary for a more accurate electronic thermomechanical model at ultra-fast timescales. This may perhaps be more impactful when studying the effects on emissions as opposed to survivability.

Additionally, the electron-phonon coupling was weak compared to the value we used for low electron temperatures and increased for increasing electron temperatures. However, the high electron temperatures were so short-lived that much of the lattice heating occurred when coupling was weak. Improving this would also decrease the observed lattice temperatures (see Appendix C), indicating that there must be more ways to heat the lattice near the apex.

One process which would lead to higher surface temperatures would be direct deposition of energy into the lattice by the nonthermal electrons. If this is a strong enough process, then the lattice temperature may increase much more quickly before the electrons may disperse the energy via electron-phonon coupling, followed by electronic cooling. As the lattice is less capable of dispersing energy, this may lead to damage.

Finally, we would like to improve upon the electron heating mechanisms. The dominant heating mechanisms vary depending on the configuration of the system. Modeling the surface as a solid density plasma, which is appropriate at such high surface fields, would invoke the normal skin effect, anomalous skin effect, high-frequency skin effect and sheath inverse bremsstrahlung [24]. All these listed improvements will serve to more accurately model these structures, their emissions and their viability as long-lifetime cathodes.

Author Contributions: Conceptualization, J.M. and J.R.; methodology, J.M.; software, J.M.; validation, J.M.; formal analysis, J.M.; investigation, J.M.; resources, J.M. and J.R.; data curation, J.M.; writing—original draft preparation, J.M.; writing—review and editing, J.R.; visualization, J.M.; supervision, J.R.; project administration, J.R.; funding acquisition, J.R. All authors have read and agreed to the published version of the manuscript.

Funding: This research was supported by the Center for Bright Beams, U.S. National Science Foundation grant PHY-1549132.

Data Availability Statement: Data and code are available upon reasonable request.

Conflicts of Interest: The authors declare no conflict of interest.

Appendix A. Mesh and Simulation Size

One concern we had was whether the simulation size was large enough. If the heat bath is too close to the apex, one then underestimates the peak temperatures achieved. Thus, we doubled the height of the structure and compared the output to our presented output (for a smaller range of angles). This comparison is shown in Figure A1. The error due to the height of the structure is worsened for smaller angles. However, by using the smaller structure throughout this study, we only underestimate the peak temperatures by up to 33.5 K for the blades and 23.3 K for the tips, which we find to be acceptable.

Another concern we had was the large grid size for the tip at the apex. We further refined the tip mesh size at the apex by a factor of 0.25 and the tangent point by 0.5. A comparison to the unrefined structure is shown in Figure A2. Luckily, by using the unrefined tip structure, we only underestimate the peak temperatures achieved by about 10 K, which we also find to be suitable.

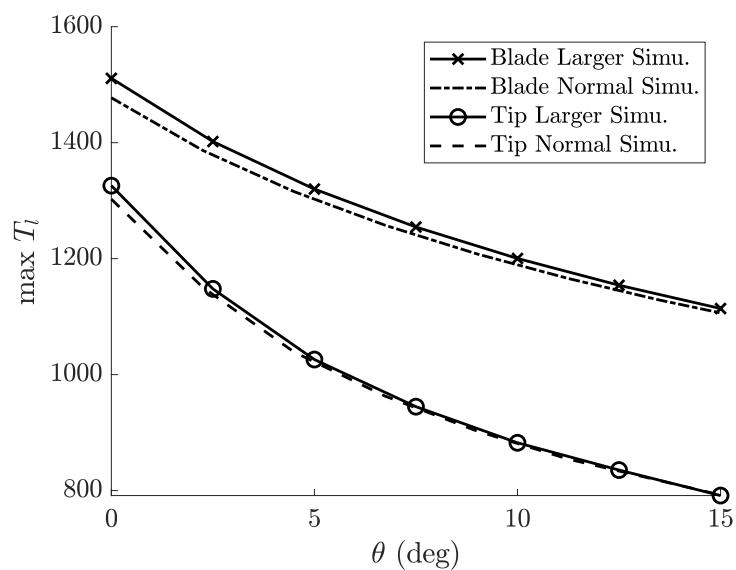


Figure A1. Comparison of tip and blade structures when doubling the height of the center of the apex circle. This moves the 300 K heat bath farther away from the apex, slightly increasing the peak achieved temperatures.

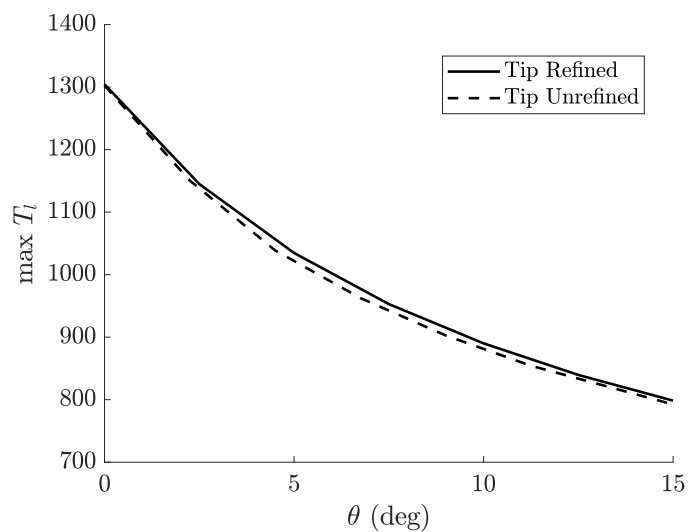


Figure A2. Comparison of the tip structure with no refinement (grid size of $0.5R$ throughout) and with refinement ($0.5 \times R$ from the apex, $0.25 \times R$ at the tangent point and $0.125R$ at the apex). Surprisingly, this refinement shows little effect on the results, only being off by up to about 10 K.

Appendix B. Comments on the Nottingham Effect

The Nottingham effect is an inevitable result of field emission. Electrons in the metal at higher normal energies, and therefore typically at higher total energies, will have a higher probability of tunneling than their lower energy counterparts within the Fermi–Dirac distribution. For a material with a nonzero temperature, this means that electrons above the Fermi level tunnel more readily than those below it, leading to a net loss of energy for the whole system.

For strong enough fields, however, the strong sampling at all energies and the relatively low population above the Fermi level lead to heating instead. The inversion temperature is the point of transition between these two regimes and is related to the field emission decay width, where $T^* = d/(2k_b)$. At 80 V/nm, the inversion temperature is approximately 20,000 K. The average energy taken away by an emitted electron is [25]

$$\mathcal{E}_e = -\pi k_b T_e \cot \frac{\pi T_e}{2 T^*} \tag{A1}$$

At the higher electron temperatures observed in this analysis, where $T_e \sim 30,000$ K, we find that each emitted electron cools the surface by 8.1 eV, whereas at 300 K, each electron heats the surface by 3.4 eV. These values are much lower than the ponderomotive energy of the field, which underpins the vacuum heating process, valued at about 50 eV.

Finally, most of the electrons that participated in the ponderomotive motion return to the metal due to a combination of the nature of surface rescattering and the collective image force [8]. This drives vacuum heating’s nonlinear behavior and comparatively inhibits the Nottingham effect. For these reasons, we omitted the Nottingham effect.

Appendix C. Reduced Electron-Phonon Coupling

Here, we consider what effect using a decreased electron-phonon coupling constant, g , would have on this analysis. Here, we choose a low-temperature value of $g = 0.2 \times 10^{17} \text{ Wm}^{-3}\text{K}^{-1}$. A comparison of the structures (equivalent to Figure 5) is shown in Figure A3. The performance hierarchy of the structures remains unchanged, with the 3-degree tip attaining a higher temperature than the 30-degree blade. As expected, the peak lattice temperatures achieved are found to be substantially lower as more energy was dissipated by the electron distribution instead of being deposited into the lattice.

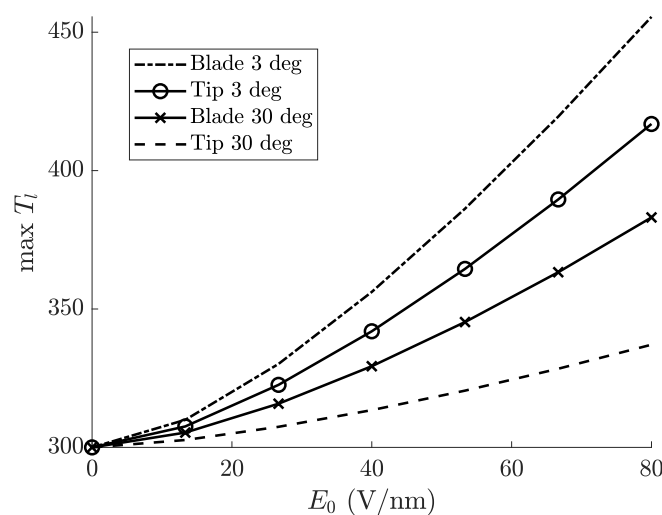


Figure A3. The peak lattice temperatures achieved as a function of the peak applied field, using the low-temperature electron-phonon coupling constant $g = 0.2 \times 10^{17} \text{ Wm}^{-3}\text{K}^{-1}$. The conclusions drawn are unchanged. The 3-degree tip (solid and circles) reaches a higher temperature than the 30-degree blade (solid and crosses). The 30-degree tip (dashed) outperforms the other structures here, and the fictional 3-degree blade (dot-dashed) represents the worst performer.

References

1. Bormann, R.; Strauch, S.; Schäfer, S.; Ropers, C. An ultrafast electron microscope gun driven by two-photon photoemission from a nanotip cathode. *J. Appl. Phys.* **2015**, *118*, 173105. [[CrossRef](#)].
2. Storeck, G.; Vogelgesang, S.; Siviš, M.; Schäfer, S.; Ropers, C. Nanotip-based photoelectron microgun for ultrafast LEED. *Struct. Dyn.* **2017**, *4*, 044024. [[CrossRef](#)] [[PubMed](#)].
3. Schröder, B.; Siviš, M.; Bormann, R.; Schäfer, S.; Ropers, C. An ultrafast nanotip electron gun triggered by grating-coupled surface plasmons. *Appl. Phys. Lett.* **2015**, *107*, 231105. [[CrossRef](#)].
4. Krüger, M.; Lemell, C.; Wachter, G.; Burgdörfer, J.; Hommelhoff, P. Attosecond physics phenomena at nanometric tips. *J. Phys. B At. Mol. Opt. Phys.* **2018**, *51*, 172001. [[CrossRef](#)].
5. Bormann, R.; Gulde, M.; Weismann, A.; Yalunin, S.V.; Ropers, C. Tip-enhanced strong-field photoemission. *Phys. Rev. Lett.* **2010**, *105*, 147601. [[CrossRef](#)] [[PubMed](#)].
6. Paschen, T.; Roussel, R.; Seiffert, L.; Kruse, B.; Heide, C.; Dienstbier, P.; Mann, J.; Rosenzweig, J.; Fennel, T.; Hommelhoff, P. Ultrafast strong-field electron emission and collective effects at a one-dimensional nanostructure. *ACS Photonics* **2023**, *10*, 447–455. [[CrossRef](#)].
7. Lawler, G.E.; Majernik, N.; Mann, J.I.; Montanez, N.E.; Rosenzweig, J.B.; Yu, V.S. Emittance measurements of nanoblade-enhanced high field cathode. In Proceedings of the IPAC'22, International Particle Accelerator Conference, Bangkok, Thailand, 12–17 June 2022; Zimmerman, F., Tanaka, H., Sudmuang, P., Klysubun, P., Sunwong, P., Chanwattana, T., Petit-Jean-Genaz, C., Schaa, V.R.W., Eds.; JACoW Publishing: Geneva, Switzerland, 2022; pp. 709–712. [[CrossRef](#)].
8. Mann, J.I.; Wang, B.; Lawler, G.E.; Rosenzweig, J.B.; Karkare, S.; Nangoi, J.K.; Arias, T. Simulations of nanoblade cathode emissions with image charge trapping for yield and brightness analyses. In Proceedings of the NAPAC'22, International Particle Accelerator Conference, Albuquerque, NM, USA, 7–12 August 2022; Biedron, S., Simakov, E., Milton, S., Anisimov, P.M., Schaa, V.R.W., Eds.; JACoW Publishing: Geneva, Switzerland, 2022; pp. 535–538. [[CrossRef](#)].
9. Mann, J.; Rosenzweig, J. Thermodynamic study of ultrafast laser-field emission at nanostructured cathodes. In Proceedings of the IPAC'23, 14th International Particle Accelerator Conference, Venice, Italy, 7–12 May 2023; Assmann, R., McIntosh, P., Bisoffi, G., Fabris, A., Andrian, I., Vinicola, G., Eds.; JACoW Publishing: Geneva, Switzerland, 2023; pp. 1600–1603. [[CrossRef](#)].
10. Dubi, Y.; Sivan, Y. 'Hot' electrons in metallic nanostructures—Non-thermal carriers or heating? *Light Sci. Appl.* **2019**, *8*, 89. [[CrossRef](#)] [[PubMed](#)].
11. Maxson, J.; Musumeci, P.; Cultrera, L.; Karkare, S.; Padmore, H. Ultrafast laser pulse heating of metallic photocathodes and its contribution to intrinsic emittance. *Nucl. Instrum. Methods Phys. Res. A Accel. Spectrom. Detect. Assoc. Equip.* **2017**, *865*, 99–104. [[CrossRef](#)].
12. Kittel, C. *Introduction to Solid State Physics*; John Wiley & Sons, Inc.: Hoboken, NJ, USA, 2005; p. 146. Available online: <https://archive.org/details/IntroductionToSolidStatePhysics> (accessed on 25 November 2023).
13. Lin, Z.; Zhigilei, L.V.; Celli, V. Electron-phonon coupling and electron heat capacity of metals under conditions of strong electron-phonon nonequilibrium. *Phys. Rev. B* **2008**, *77*, 075133. [[CrossRef](#)].
14. Kakemoto, H. Theoretical specific heat, and thermal conductivity estimated by detailed phonon vibrations. *ACS Appl. Electron. Mater.* **2019**, *1*, 2476–2482. [[CrossRef](#)].
15. Cahill, D.G.; Watson, S.K.; Pohl, R.O. Lower limit to the thermal conductivity of disordered crystals. *Phys. Rev. B* **1992**, *46*, 6131–6140. [[CrossRef](#)].
16. Lide, D.R. (Ed.) *CRC Handbook of Chemistry and Physics*; CRC Press LLC: Boca Raton, FL, USA, 2003; Chapter 14. Available online: <https://zlibrary.to/filedownload/crc-handbook-of-chemistry-and-physics-3> (accessed on 25 November 2023).
17. Magnozzi, M.; Ferrera, M.; Mattera, L.; Canepa, M.; Bisio, F. Plasmonics of Au nanoparticles in a hot thermodynamic bath. *Nanoscale* **2018**, *11*, 1140–1146. [[CrossRef](#)] [[PubMed](#)].
18. Ren, Y.; Chen, J.K.; Zhang, Y.; Huang, J. Ultrashort laser pulse energy deposition in metal films with phase changes. *Appl. Phys. Lett.* **2011**, *98*, 191105. [[CrossRef](#)].
19. Brunel, F. Not-so-resonant, resonant absorption. *Phys. Rev. Lett.* **1987**, *59*, 52–55. [[CrossRef](#)] [[PubMed](#)].
20. Wilson, G.; Dennison, J.R. Approximation of range in materials as a function of incident electron energy. *IEEE Trans. Plasma Sci.* **2012**, *40*, 291–297. [[CrossRef](#)].
21. Geuzaine, C.; Remacle, J.F. Gmsh: A 3-D finite element mesh generator with built-in pre- and post-processing facilities. *Int. J. Numer. Methods Eng.* **2009**, *79*, 1309–1331. [[CrossRef](#)].
22. Cimrman, R.; Lukeš, V.; Rohan, E. Multiscale finite element calculations in Python using SfePy. *Adv. Comput. Math.* **2019**, *45*, 1897–1921. [[CrossRef](#)].
23. Brau, C.A. *Proposal for Research on High-Brightness Cathodes for High-Power Free-Electron Lasers (FEL)*; Final Report; Vanderbilt University, Division of Sponsored Research: Nashville, TN, USA, 2013. Available online: <https://apps.dtic.mil/sti/tr/pdf/ADA580721.pdf> (accessed on 25 November 2023).
24. Rozmus, W.; Tikhonchuk, V.T.; Cauble, R. A model of ultrashort laser pulse absorption in solid targets. *Phys. Plasmas* **1996**, *3*, 360–367. [[CrossRef](#)].
25. Paulini, J.; Klein, T.; Simon, G. Thermo-field emission and the Nottingham effect. *J. Phys. D Appl. Phys.* **1993**, *26*, 1310–1315. [[CrossRef](#)].

Disclaimer/Publisher's Note: The statements, opinions and data contained in all publications are solely those of the individual author(s) and contributor(s) and not of MDPI and/or the editor(s). MDPI and/or the editor(s) disclaim responsibility for any injury to people or property resulting from any ideas, methods, instructions or products referred to in the content.